

Supplementary Material

**Understanding the Carbonization-Controlled Microstructure
Regulation in Coal-Base Hard Carbon for Strengthen Sodium
Storage Performance**

Yu Zhao ^{a†}, Ruyi Zhang ^{a†}, Jian Hao ^{a*}, XiaoYang ^a, Jianing Chen ^a,
Junli Guo ^{b*}, Caixia Chi ^c

^a *College of Chemistry & Chemical Engineering, State Key Laboratory of High-efficiency Utilization of Coal and Green Chemical Engineering, Ningxia University, Yinchuan 750021, China. E-mail: haojian2017@126.com*

^b *College of Mechanical Engineering, Ningxia University, Yinchuan 750021, China.*

^c *Heilongjiang Province Key Laboratory of Environmental Catalysis and Energy Storage Materials, Suihua 152061, China.*

[†]*These authors contributed equally to this work.*

Table S1 The carbon yield of samples

Samples	MC-700	MC-800	MC-900	MC-1000	MC-1100	MC-900-1	MC-900-10
Yield	65%	62%	60%	57%	52%	58%	61%

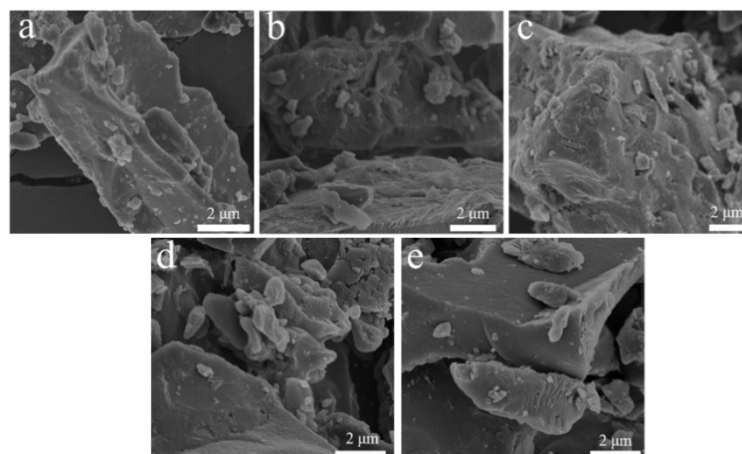


Figure S1 SEM images of (a) MC-700, (b) MC-800, (c) MC-900, (d) MC-1000, (e) MC-1100.

Table S2 Physical parameters of XRD and Raman of samples

samples	2θ (°)	d_{002} (nm)	A_{D1}/A_G
MC-700	22.713	0.391	1.9
MC-800	23.006	0.386	1.84
MC-900	23.189	0.383	1.8
MC-1000	23.370	0.380	1.71
MC-1100	23.505	0.378	1.62

Table S3 Percentage of various functional groups in different samples

samples	C=C	C-O	C=O
MC-700	56.1%	9.1%	15.2%
MC-900	66.7%	6.9%	12.8%
MC-1100	73.9%	5.7%	8.7%

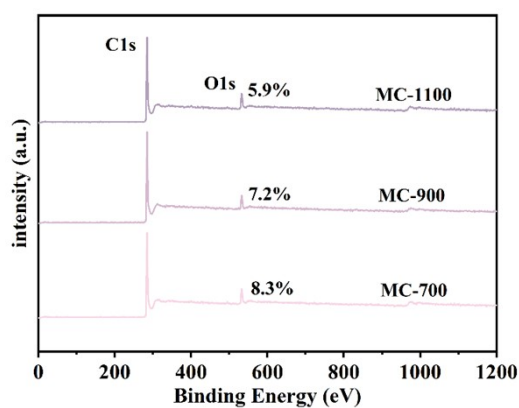


Figure S2 XPS survey spectrum of MC-700, MC-900 and MC-1100.

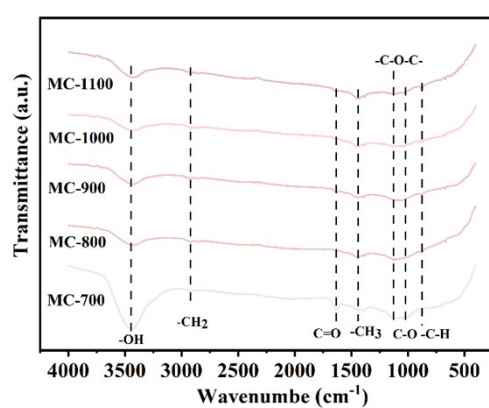


Figure S3 FTIR spectra of MC-X.

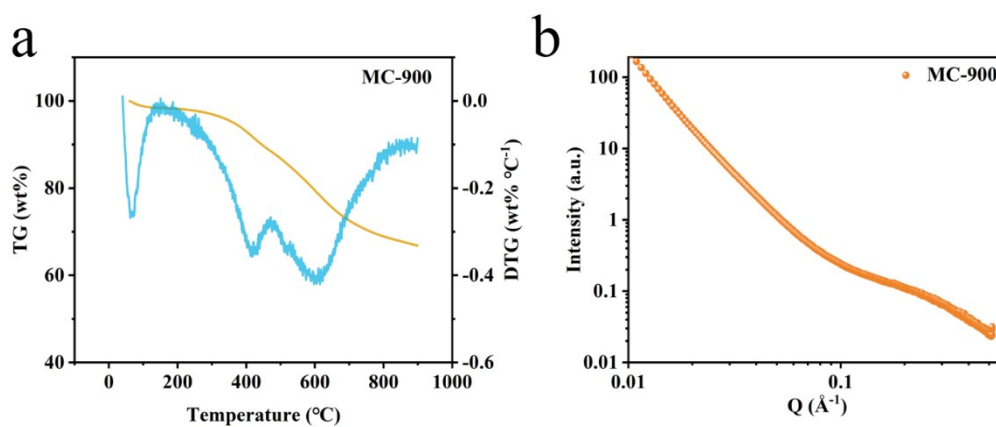


Figure S4 The TG and DTG curves (a) and SAXS pattern (b) of MC-900.

Table S4 Pore size structure of samples

samples	S_{BET} ($\text{m}^2 \text{g}^{-1}$)	V_{total} ($\text{cm}^3 \text{g}^{-1}$)	V_{micro} ($\text{cm}^3 \text{g}^{-1}$)	$V_{\text{micro}}/V_{\text{total}}$ (%)
MC-700	312.30	0.18	0.13	72.2
MC-900	256.75	0.16	0.09	56.3
MC-1100	188.67	0.13	0.06	46.2

V_{total} : Total pore volume; V_{micro} : Micropore volume; $V_{\text{micro}}/V_{\text{total}}$: Proportion of micropore volume to total pore

volume.

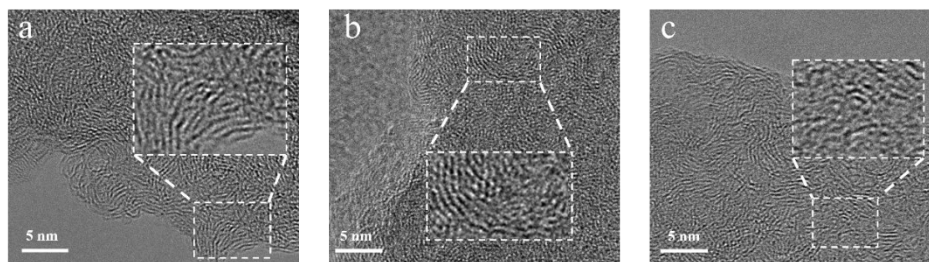


Figure S5 TEM images (a) MC-900-1, (b) MC-900, (c) MC-900-10, inset magnification is 2x.

Figure S5 shows that MC-900-10 has the smallest graphite microcrystalline structure and a higher proportion of amorphous regions, while MC-900-1 contains more graphite microcrystals, featuring a larger structure and increased pseudo-graphite regions.

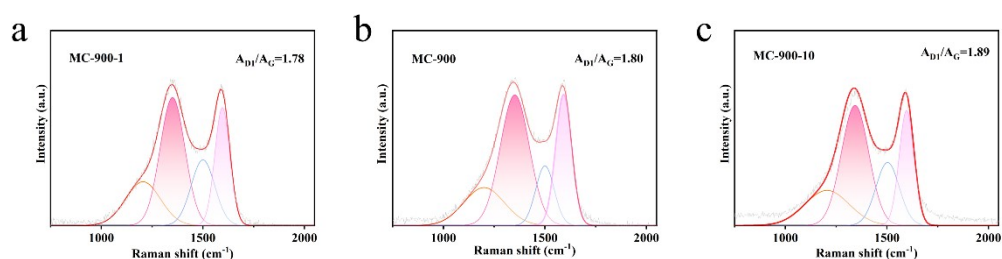


Figure S6 Raman spectra of MC-900-1, MC-900 and MC-900-10.

The fitted Raman spectrum is shown in Figure S6. The A_{D1}/A_G values were calculated as follows: MC-900-1: 1.78, MC-900: 1.80, and MC-900-10: 1.89. It is evident that as the heating rate increases, the A_{D1}/A_G value gradually rises, indicating that a faster heating rate leads to less complete carbonization of the coal-based materials.

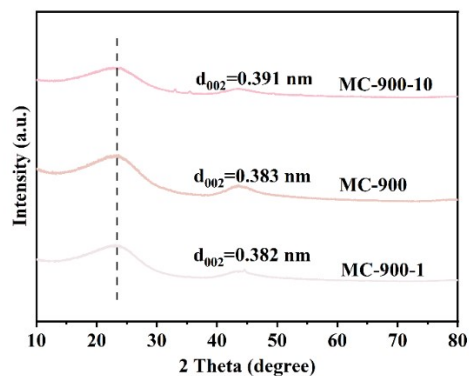


Figure S7 XRD patterns of MC-900-1, MC-900, and MC-900-10.

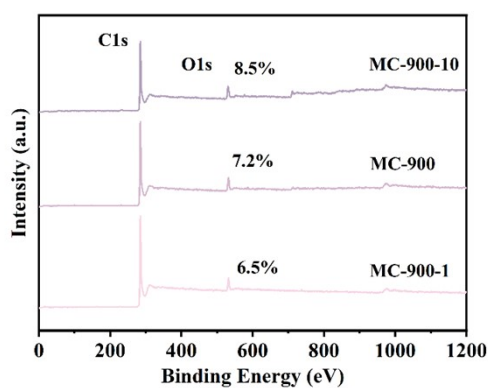


Figure S8 XPS survey spectrum of MC-900-1, MC-900 and MC-900-10.

It can be seen from Figure S8 that as the heating rate decreases, the oxygen content inside the sample decreases from 8.5% of MC-900-10 to 6.5% of MC-900-1, indicating that a slower heating rate will reduce the oxygen content inside the samples.

Table S5 Percentage of various functional groups in different samples

samples	C=C	C-O	C=O
MC-900-1	52.9%	14.4%	12.4%
MC-900	66.7%	6.9%	12.8%
MC-900-10	44.5%	19.7%	11.8%

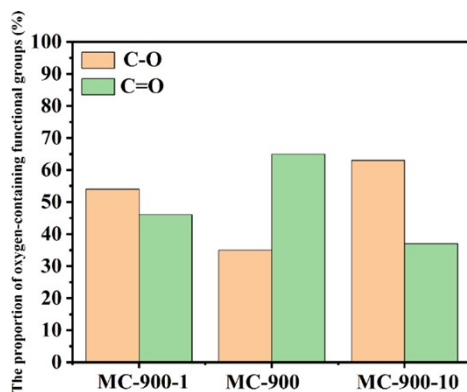


Figure S9 The proportion of different oxygen-containing functional groups inside the samples.

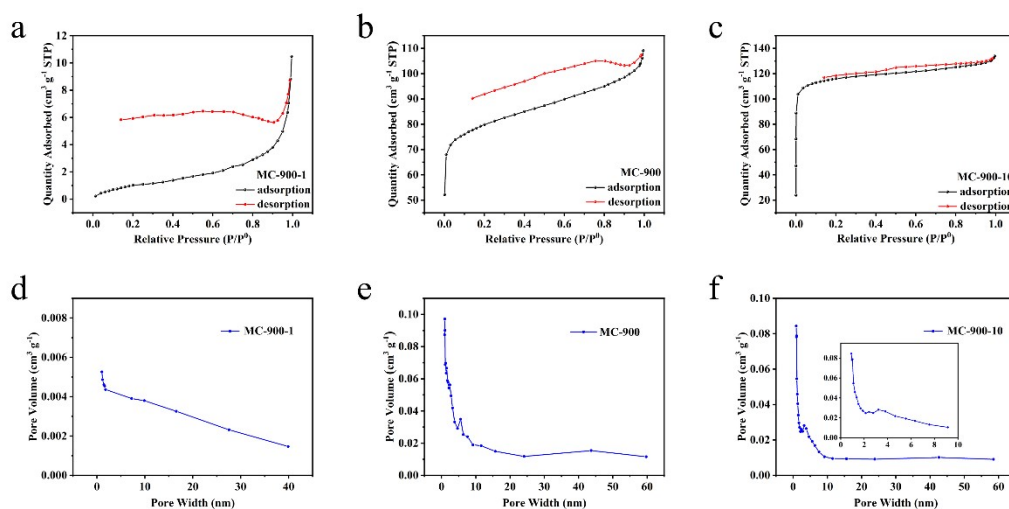


Figure S10 Nitrogen adsorption and desorption curves of (a) MC-900-1, (b) MC-900, (c) MC-900-10, pore size distribution of (a) MC-900-1, (b) MC-900, (c) MC-900-10.

Table S6 Pore size structure of samples

samples	$S_{\text{BET}}/(\text{m}^2 \text{g}^{-1})$	$V_{\text{total}}(\text{cm}^3 \text{g}^{-1})$	$V_{\text{micro}}(\text{cm}^3 \text{g}^{-1})$	$V_{\text{micro}}/V_{\text{total}}(\%)$
MC-900-1	366.45	0.20	0.15	75.0
MC-900	256.75	0.16	0.09	56.3
MC-900-10	4.39	0.014	0.001	7.1

V_{total} : Total pore volume; V_{micro} : Micropore volume; $V_{\text{micro}}/V_{\text{total}}$: Proportion of micropore volume to total pore volume.

Figure S10 presents the N_2 adsorption-desorption isotherms and pore size distribution curves for samples at different heating rates. The N_2 adsorption-desorption isotherm of MC-900-10 shows a Type I pattern, which indicates that the material

mainly consists of micropores. In addition, the specific surface areas of MC-900-1, MC-900 and MC-900-10 are 4.39, 256.75 and 366.45 $\text{m}^2 \text{g}^{-1}$ respectively (Table S6).

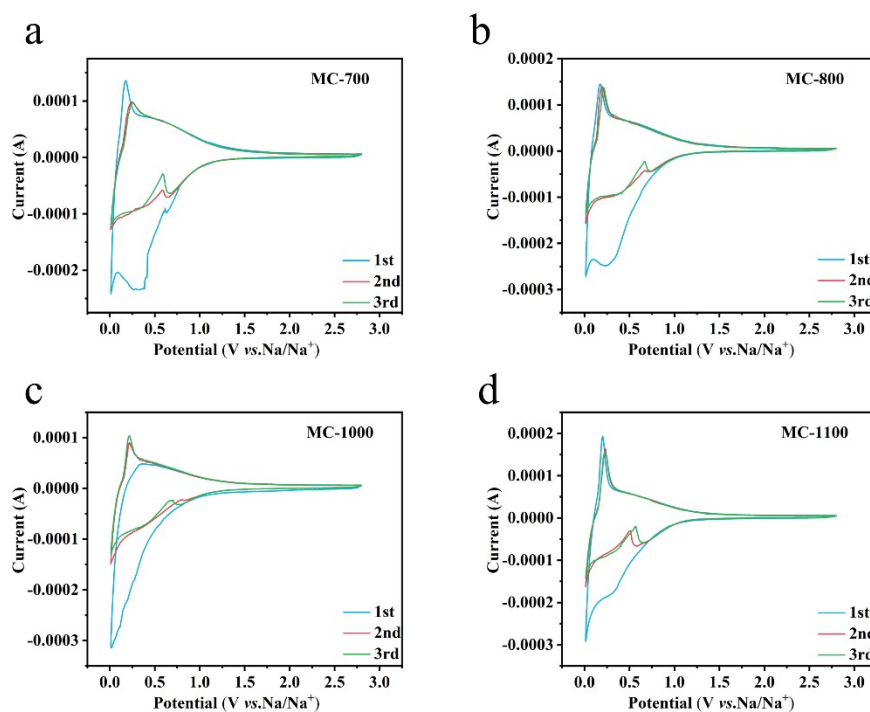


Figure S11 Cyclic voltammetry curve of (a) MC-700, (b) MC-800, (c) MC-1000, (d) MC-1100.

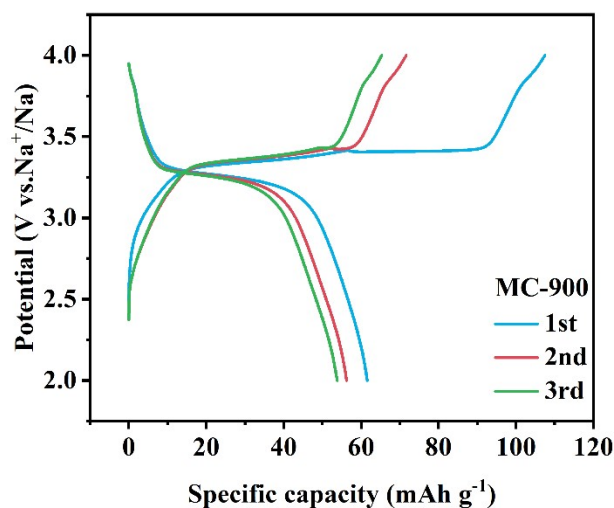


Figure S12 The GCD curves of NVP | MC-900 full-cell at 0.1C.

The full-cell tests employed an anode with 1.1 mg cm^{-2} active material loading and a $\text{Na}_3\text{V}_2(\text{PO}_4)_3$ (NVP) cathode (10 mg cm^{-2} loading, 93.5% active material ratio).

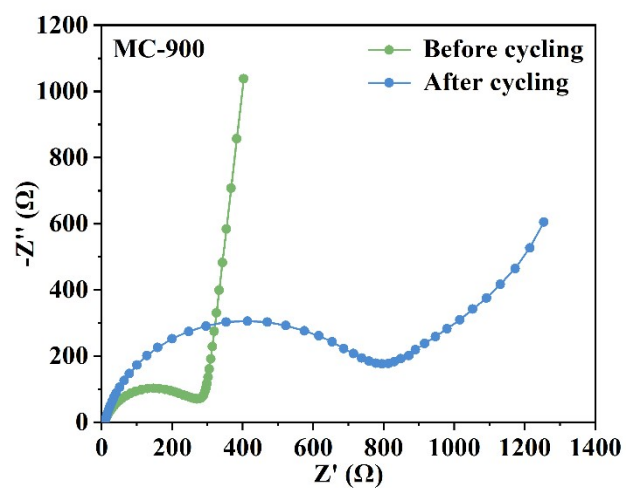


Figure S13 EIS spectra of MC-900 before and after electrochemical testing.

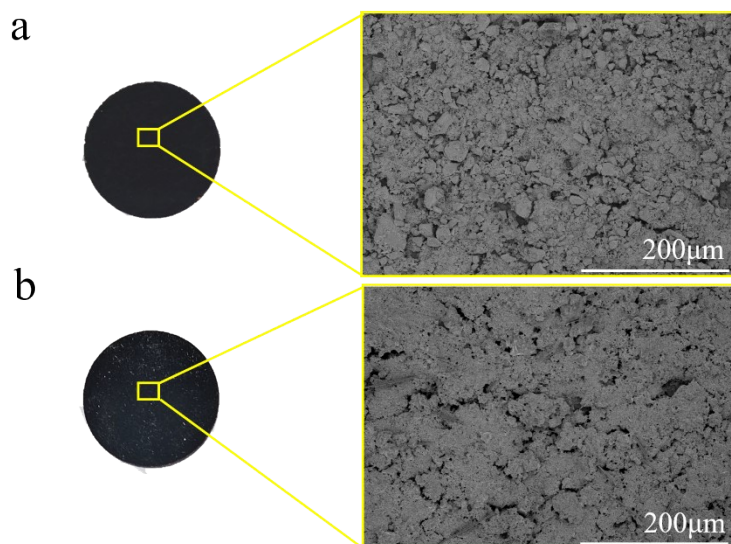


Figure S14 Optical and SEM images of the electrode before and after electrochemical testing: (a) before cycling, (b) after cycling.

Table S7 Electrochemical performances of reported coal-based hard carbon anode materials for

SIBs				
Materials	strategy	Capacity (mAh g ⁻¹)	Cyclability (mAh g ⁻¹)	Year/Ref
anthracite	Introduction of NH ₃	286 at 0.05 A g ⁻¹	220 at 0.1 A g ⁻¹ after 500 cycles	2023 ²³
anthracite	Nitrogen-Doping	323 at 0.03 A g ⁻¹	192 at 1.0 A g ⁻¹ after 1000 cycles	2024 ²⁴
Bituminous coal	Zn ₂ (OH) ₂ CO ₃ assisted ball milling pretreatment	325.3 at 0.03 A g ⁻¹	226.1 at 0.1 A g ⁻¹ after 500 cycles	2024 ²⁵
Bituminous coal	molten salt-assisted approach	303.6 at 0.03 A g ⁻¹	82.1 at 0.5 A g ⁻¹ after 1000 cycles	2024 ²⁶
Long-flame coal	carbonization	254 at 0.02 A g ⁻¹	159 at 0.5 A g ⁻¹ after 1000 cycles	2025 ²⁷
lignite	low-temperature pyrolysis	282.9 at 0.02 A g ⁻¹	51.5 at 0.5 A g ⁻¹ after 500 cycles	2025 ²⁸
Bituminous coal	liquid-phase surface coating	326.7 at 0.02 A g ⁻¹	62.8 at 0.2 A g ⁻¹ after 2000 cycles	2025 ²⁹

Table S8 Impedance parameters of samples

Samples	R _s (Ω)	R _{ct} (Ω)	CPE _{1-T}	CPE _{1-P}	σ (Ω s ^{-1/2})	D _{Na+} (cm ² s ⁻¹)
MC-700	6.73	615.7	5.96×10 ⁻⁶	0.91	342.0	4.565×10 ⁻¹⁵
MC-800	6.01	496.9	7.94×10 ⁻⁶	0.88	222.5	1.079×10 ⁻¹⁴
MC-900	6.44	222.8	2.29×10 ⁻⁵	0.84	72.1	1.027×10 ⁻¹³
MC-1000	4.35	339.6	1.06×10 ⁻⁵	0.85	119.3	3.752×10 ⁻¹⁴
MC-1100	4.13	259	1.183×10 ⁻⁵	0.87	273.7	7.128×10 ⁻¹⁵

Note: R_s: ohmic resistance; R_{ct}: transfer resistance.

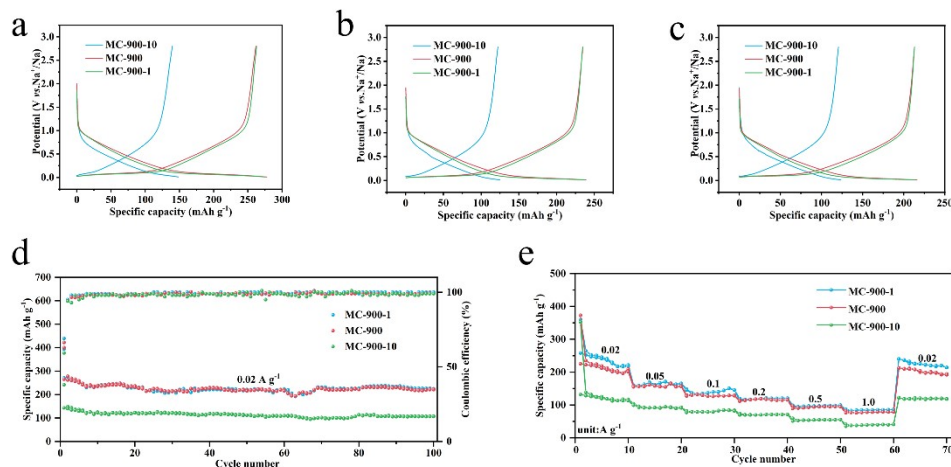


Figure S15 The constant current charge-discharge curve of MC-900-1, MC-900 and MC-900-10 at 0.02 A g^{-1} , (a) 2nd, (b) 10th, (c) 30th, (d) cycling performance of MC-900-1, MC-900 and MC-900-10 at the current density of 0.02 A g^{-1} , (e) rate performance of MC-900-1, MC-900 and MC-900-10.

Figure S15a-c presents the GCD curves of MC-900-1, MC-900 and MC-900-10 at a current density of 0.02 A g^{-1} . It is evident that MC-900-10 exhibits the lowest plateau capacity (40.58 mAh g^{-1}). The cycling performance of MC-900-1, MC-900, MC-900-10 is illustrated in Figure S15d. After 100 cycles, the discharge specific capacities of MC-900-1 and MC-900 are 224.28 and $223.19 \text{ mAh g}^{-1}$, respectively. Figure S15e presents the rate performance of MC-900-1, MC-900, MC-900-10. As the current density increases from 0.1 A g^{-1} to 1 A g^{-1} , the MC-900 demonstrates the highest capacity retention rate (62.3%).

Table S9 Specific capacity (mAh g^{-1}) of the slope region at different cycle numbers

Cycle numbers	MC-700	MC-900	MC-1100
2nd	128.04	165.94	102.2
10th	118.64	140.2	93.55
50th	105.95	130.75	77.77